PCCP

PAPER

View Article Online
View Journal | View Issue

Cite this: *Phys. Chem. Chem. Phys.*, 2026, **28**, 3613

Defect chemistry manipulation by heavy ion irradiation in Y-doped CeO_2 solid solutions

R. Mohun, *[a] T. Cordara,[b] J. McCloy,[c] M. H. Weber,[c] S. C. Middleburgh[a] and C. L. Corkhill[d]

Received 16th May 2025,
Accepted 14th October 2025

DOI: 10.1039/d5cp01848j

rsc.li/pccp

A combination of experimental methods is used to study the effect of trivalent cation doping and radiation stability of Y-doped CeO_2 with dopant content ranging from 0–15 wt%. X-ray diffraction reveals that Y-incorporation leads to long-range ordering of anionic vacancies with randomly distributed C-type Y_2O_3 nanodomains that form coherently within the host fluorite structure. Raman and positron annihilation spectroscopies are employed to characterise and analyse the nature of oxygen vacancies that charge the aliovalent direct substitution and Ce^{3+} formation. Heavy-ion irradiation at different fluences (1×10^{16} and 5×10^{16} ions per cm^2) shows that the doped compositions offer improved resistance to radiation damage. These findings are attributed to the ballistic mixing of dopant-induced defects with those introduced by ionic implantation, thereby increasing defect recombination volume and enhancing lattice recovery. Furthermore, the defect migration and annealing mechanisms are seen to differ for the studied fluences, highlighting the specific role of sample surfaces as effective annealing sites.

1. Introduction

The defect structure of doped fluorite-type materials, including CeO_2, UO_2 and PuO_2, is of critical importance to energy applications. For instance, the development of low temperature solid oxide fuel cell (SOFC) technologies in the last decade has focused on investigating the properties of trivalent rare-earth element doped CeO_2 materials.[1,2] Due to their aliovalent charge, oxygen vacancies are formed as a charge compensation mechanism when trivalent elements are introduced into the CeO_2 lattice. Owing to the enhanced oxygen diffusion afforded by the presence of these anionic defects, the ionic conductivity of doped CeO_2 is improved and tends to increase with increasing trivalent rare-earth concentration, to a maximum at between ~5 and 20 mol%, depending on the temperature and the ion concerned.[3]

In the context of nuclear energy, trivalent rare earth elements are found in solid solution with UO_2 upon nuclear fission, and soluble species such as Gd^{3+} are being explored as neutron poisons for incorporation within mixed $(U,Pu)O_2$ for disposal of the UK's plutonium stockpile.[4] Trivalent cations modify the UO_2 structure, through the induction of pentavalent uranium and/or oxygen vacancies,[5] which can significantly alter the long-term stability of used fuel. Thus, determining the defect structure of these materials and how it may be manipulated are of great interest for developing engineered facilities for long-term nuclear waste management as well as SOFC technologies, as previously mentioned.

For these reasons, we investigate the effects of irradiation, using ion implantation techniques, on the defect chemistry of Y-doped CeO_2 fluorite materials. Since the ionic conductivity of doped CeO_2 is limited by the formation of nano-domains of rare earth oxide elements,[6–10] ion implantation offers an alternative route to enhance conductivity for low temperature SOFC applications. Despite a number of studies devoted to characterising the irradiation behaviour of UO_2,[11,12] the defect chemistry of trivalent cation doped UO_2 during irradiation is not well understood. CeO_2, with a fluorite $Fm\bar{3}m$ crystallographic structure, consists of a simple cubic oxygen sublattice with the cation ions occupying alternate cube centres, offering an elegant surrogate to UO_2 and PuO_2 to investigate these effects.[13–16] We present an in-depth experimental study to characterise the defect structures of Y-doped CeO_2 systems with Y-contents ranging from 0 to 15 wt%, followed by irradiation with heavy Au ions.

[a] *Nuclear Futures Institute, School of Computer and Science Engineering, Bangor University, Bangor, LL57 1UT, UK. E-mail: r.mohun@bangor.ac.uk*
[b] *ISL, The University of Sheffield, Sir Robert Hadfield Building, Mappin Street, Sheffield, S1 3JD, UK*
[c] *Center for Materials Research, Washington State University, Pullman, WA, 99164, USA*
[d] *School of Earth Sciences, University of Bristol, Queens Road, Bristol, BS8 1RH, UK*

2. Experimental

2.1 Material synthesis

Y-doped CeO_2 with various compositions was synthesised *via* an oxalic precipitation route within the HADES facility at the

University of Sheffield.[17] Solutions of $CeCl_3$ (1.0 M) and YCl_3 (0.1 M) were first prepared by dissolving the required amounts of $CeCl_3{\cdot}6H_2O$ (>99.9%; Sigma Aldrich) and $YCl_3{\cdot}6H_2O$ (>99.9%; Sigma Aldrich) in hydrochloric acid (1 M, Sigma Aldrich). Around 1 gram of each targeted composition was aimed by mixing stoichiometric volumes of the Ce and dopant solutions using high-accuracy Sigma Aldrich PIPETMAN micropipettes. Oxalate hydrates were precipitated by adding excess oxalic acid (1 M, Sigma Aldrich & 1 : 15 volume ratio) to the solutions, washed twice with deionised water and washed a final time with ethanol. All precipitates were dried overnight at 90 °C and calcined at 1000 °C for 4 hours in air to produce oxide powders. The obtained powders were planetary milled for 30 minutes, uniaxially pressed into 10 mm diameter pellets under a force of 520.34 MPa and a holding time of 4 minutes. The green pellets were then sintered at 1700 °C for 10 hours in air.

2.2 Sample irradiation and characterisation

Heavy-ion irradiation experiments were carried out at the Helmholtz–Zentrum Dresden–Rossendorf (HZDR) facility in Germany. Sintered pellets were irradiated with 3 MeV Au-ions at room temperature at fluences of 1×10^{15} and 5×10^{15} ions per cm^2, which correspond to a maximum defect concentration of 5.64 and 28.2 displacements per Au-ion (dpa) in the sample bulk, respectively.[18] These conditions were chosen to simulate the ballistic regime of fission products in nuclear fuels. The sample holder was continuously cooled to avoid local heating effects during ionic implantation and characterisation techniques were performed on the irradiated surfaces to analyse the damaged region. Only samples doped with 4, 8, and 15 wt% Y and a reference undoped CeO_2 were irradiated.

XRD was performed using a PANanalytical X'pert 3 diffractometer in reflection mode at 30 kV, 10 mA with Cu Kα (λ = 1.5418 Å). The scanning range was $20^\circ \leq 2\theta \leq 90^\circ$ with a step time of 5 s and a size step of 0.01°. All measurements were performed at room temperature. Lattice parameters were determined by Rietveld's analysis of the X-ray diffraction patterns using Topas software. Raman spectroscopy characterisation was performed using a Renishaw Invia Reflex confocal spectrometer. The apparatus is equipped with a 514 nm Ar(+) excitation laser and a holographic grating of 2400 lines per mm for a spectral acquisition between 200 and 800 cm^{-1}. These configurations were sufficient to allow a 2–3 cm^{-1} spectral resolution. The intensity of the only Raman-active T_{2g} mode depends on crystallographic orientation. For this reason, point measurements were carried out on different grains, with averages then taken to confirm their reproducibility and homogeneity of the composition.

Depth-resolved Doppler Broadening Positron Annihilation Spectroscopy (DBf-PAS) was performed using a slow positron beam at Washington State University, USA. This spectroscopy is based on the special properties of the positron–electron annihilation process and is specifically useful to investigate open-volume defects in materials in the near surface region to an average depth of about 5 μm (70 keV incident positron energy for a density of 7.22 g cm^{-3}). The positron–electron momentum distributions were measured at room temperature by recording the Doppler broadening of the 511 keV annihilation gamma line. A high energy resolution (1.5 keV full width at half maximum at 511 keV), high purity germanium detector (HPGe) was used. The signal was gated in coincidence with a second HPGe detector to reduce the effect of backscattering positrons which may annihilate at nearby vacuum chamber walls that without coincidence gating would cause a systematic effect. The 511 keV peak is more Doppler broadened by the longitudinal momentum of the annihilating pairs at defect sites than it would occur in the case of the annihilation with the nucleus. Thus, the broadening is more significant in a highly defective sample than in a defect-free sample. The analysis of the annihilation line can provide relevant information about defect structures. The broadened Doppler spectrum can be evaluated using the line shape (S) and wings (W) parameters. The S-parameter measures the annihilation of positrons with low-momentum electrons in the range ($|-2.177|$ to $|2.177|$) $\times$ 10^{-3} m_0c. It is related to the defects contained in a material. The W-parameter measures the annihilation of positrons with high momentum electrons in the range of ($|-24.88|$ to $|-9.64|$ and $|9.64|$ to $|24.88|$) $\times$ $10^{-3}m_0c$. The high momentum W-parameter gives information on the chemical environment of the defects. Thus, increasing the defect concentration should increase the S-parameter while decreasing the W-parameter. In this study, the average S and W values were measured with a positron beam energy ranging from 16 to 18 keV, *i.e.*, at a mean positron implantation depth of about 400 nm to avoid surface effects such as polishing defects and open porosity. The measured S and W values are determined by the material, detector resolution, and experimental design. As a result, the measured values must be normalised to a reference sample value in order to be independent of the experimental setup and comparable to other data points. In this work, the reference $S_{L(deep)}$ = 0.42154 and $W_{L(deep)}$ = 0.06818 values were measured and obtained from the bulk (*i.e.* >4 μm mean depth) of the undoped CeO_2 sample, where grains were large enough (>1 μm) to avoid detectable numbers of positrons reaching grain boundaries.

3. Results

3.1 Trivalent ion substitution in $Ce_{1-x}Y_xO_{2-(x/2)}$

X-ray diffraction showed that all samples exhibited a characteristic CeO_2 fluorite-type structure (JCPDS 34-0394) (Fig. 1), with no impurity peaks, indicating a good incorporation of the dopant into the host matrix. A close examination of the qualitative aspects of the patterns on the expanded view on the right-hand side of Fig. 1 indicates a gradual shift of the main reflection to higher angles with increasing Y-content, suggesting a compression of the unit cell volume.

In CeO_2, the cations lie at the centre of a perfect cube, coordinated with 8 oxygen ions. Upon doping, assuming that the host cations are substituted by a trivalent dopant while still maintaining the 8-fold coordination, the difference in the ionic radii of Ce/Y (r_{Ce4+} [C.N.:8] = 0.97 Å and r_{Y3+} [C.N.:8] = 1.019 Å)[19]

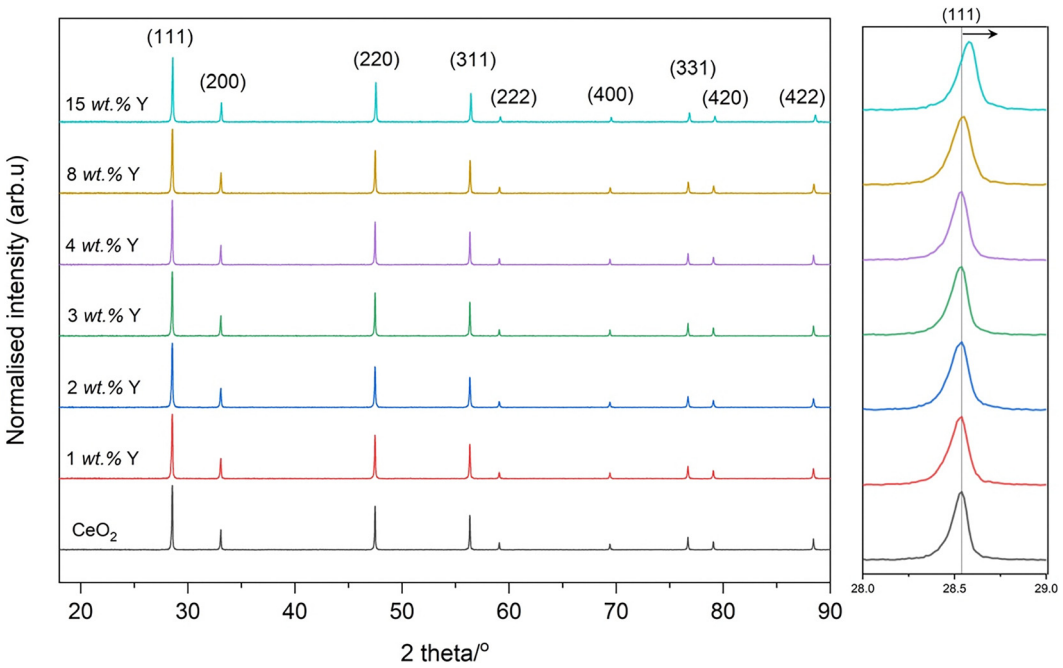

Fig. 1 X-ray diffraction patterns of as-sintered pure CeO_2 and Y-doped solid solutions showing that all compositions crystallised into the fluorite structure. The (111) reflection shifts to higher 2θ values, indicating unit cell compression shown on the right-hand side.

would suggest an expansion of the unit cell. However, the lattice parameter shows otherwise (Fig. 2). Corduri *et al.*[20] studied CeO_2 doped over a range of rare-earth elements and reported that the shrinkage of the unit cell is due to a certain long-range ordering of anionic vacancies with randomly distributed Y_2O_3 nano-domains of 'C-type' structure which grow coherently within the fluorite matrix.[21,22] The C-type configuration is very close to the CeO_2 $Fm\bar{3}m$ symmetry: it is obtained from a $2 \times 2 \times 2$ fluorite supercell by removing two oxygen ions in each of the single fluorite cells. In this way, the space group symmetry is lowered to $Ia\bar{3}$, and the cations drop to a 6-fold coordination which leads to the observed lattice parameter decrease.[23] Such C-type configurations are not apparent on the XRD patterns, even at the highest dopant concentration, indicating that their contribution is small.

Trivalent doping further alters the CeO_2 structure and increases the system complexity by inducing oxygen vacancies to compensate for the charge of the substitutional defect.

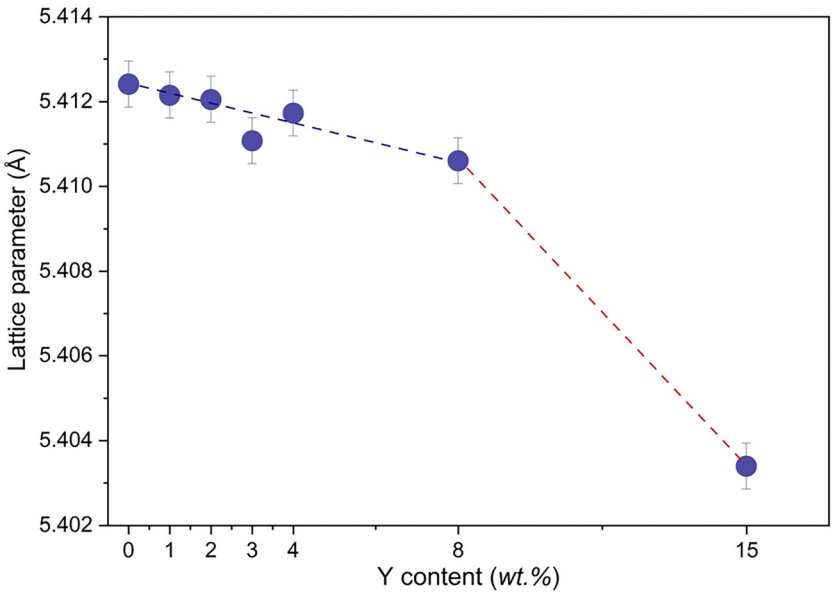

Fig. 2 Evolution of lattice parameters for undoped and doped-CeO_2 compositions highlighting the effect of trivalent doping in the host structure.

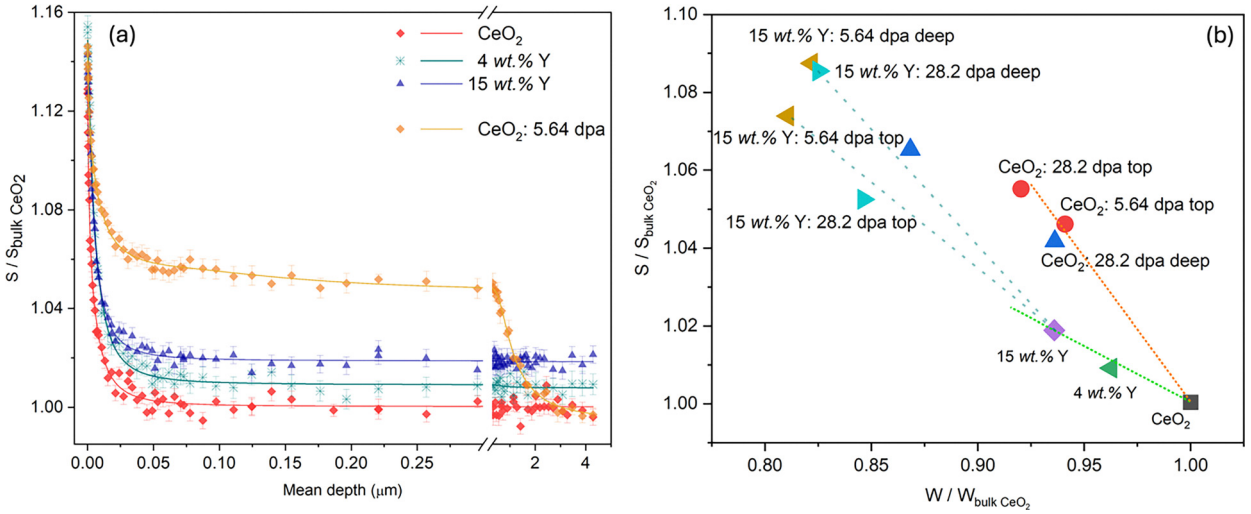

Fig. 3 (a) Relative low momentum (*S*) as a function of sample depth and (b) the evolution of the low momentum (*S*) against the high momentum (*W*) parameter (measured at depth around 400 nm) showing lattice changes caused by Y-doping (0, 4 and 15 wt%) and irradiation at low (5.64 dpa) and high (28.2 dpa) fluences.

The general evolution of the defect chemistry of CeO_2 as a function of dopant concentration was quantified using positron annihilation spectroscopy (Fig. 3). A rapid decrease in the *S*-parameter as a function of depth (up to 0.05 μm) was observed for the undoped CeO_2 indicating that the thermalised positrons diffusing toward the surface were suppressed, *i.e.*, positrons were trapped in the near surface region. The *S*-parameter then remained almost constant between 0.05 and 0.3 μm, which corresponds to the annihilation of positrons in a homogeneous CeO_2 layer. Here, positrons are implanted at a depth too great to enable diffusion back to the surface; therefore the behaviour of defects between different samples can be compared at these depths.

An increase in the low momentum *S*-parameter with dopant content is observed in agreement with an increase in lattice disorder. This is seen in the SW plot by the linear trend originating from the undoped CeO_2. This observation suggests an increase in open volume but at a lower size per defect, which can be attributed to the smaller size of Y-sites in 6-fold coordination with a resulting larger inter-atomic volume. Though positrons will not detect a positively charged isolated oxygen vacancy, they may observe defect complexes associated with oxygen vacancies that are neutrally charged, such as $\{Ce^{\bullet} - V_O'' - Ce^{\bullet}\}^X$ in undoped CeO_2 or $\{Y^{\bullet} - V_O'' - Y^{\bullet}\}^X$ or $\{Y^{\bullet} - V_O'' - Ce^{\bullet}\}^X$ in the mixed oxides. This has previously been reported, both experimentally and using first-principles calculations of positron lifetimes in UO_2, where the slope of the SW line was attributed to the so-called Schottky defects, *i.e.*, a defect complex linked with oxygen vacancies.[24]

Raman spectroscopy was then used to enable identification of these defects and other crystallographic effects of Y doping. Group theory predicts only one Raman-active (T_{2g}) optical phonon and two infrared-active optical phonons corresponding to the transverse optical (TO) and longitudinal optical (LO) modes for CeO_2. However, with an unpolarised laser and the conditions employed in this work, only the T_{2g} mode ($\sim$464 cm^{-1} for CeO_2) could be seen (Fig. 4). This Raman band is characteristic of compounds with the $Fm\bar{3}m$ space group and corresponds to the Ce–O vibration. Any microscopic mechanisms altering normal lattice vibrations will have an impact on T_{2g} parameters such as wavenumber, band shape, and intensity.

Y-incorporation induced a shift of the main T_{2g} band to higher wavenumbers, highlighting the dominant mass effect (Y^{3+}: 88.9 amu & Ce^{4+}: 140.12 amu) for the translational modes. In addition, the T_{2g} broadening, expressed in terms of full-width half maximum (FWHM), is consistent with previous results reported on rare-earth doped CeO_2. This agrees with an increased concentration of local disorder in the host matrix.[25]

A small shoulder at $\sim$370 cm^{-1} is also observed for the highest doped CeO_2. This band is the signature of the C-type configurations resulting from the (A_g + T_g) Y–O symmetrical stretching mode with Y in six-fold coordination, as revealed by XRD.[20] The intensity of this peak is dependent on the dopant content, thus underlining the long-range ordering of the C-type configuration in the fluorite lattice. A broad band also appears at $\sim$250 cm^{-1} for the highest doped sample, attributed to lattice distortions resulting from the redox properties of CeO_2 in altering the Ce^{3+}/Ce^{4+} ratio.[26] Further investigations into Ce^{3+} induction were carried out by examining the additional features seen in the 525–650 cm^{-1} spectral range. These peaks were deconvoluted in two separate regions, referred to as the D_1 ($\sim$540 cm^{-1}) and D_2 ($\sim$601 cm^{-1}) bands. Theoretical calculations by McBride *et al.*[27] revealed that D_1 occurs as a result of oxygen vacancies to maintain charge neutrality due to the substitution of a pair of Ce^{4+} ions by the trivalent dopants *i.e.*, extrinsic Y^{3+}-V_O defects (*i.e.*, $\{Y^{\bullet} - V_O'' - Ce^{\bullet}\}^X$, as predicted by PAS). Raman spectroscopy does not quantify point defects, but it can be used to characterise relevant mechanisms

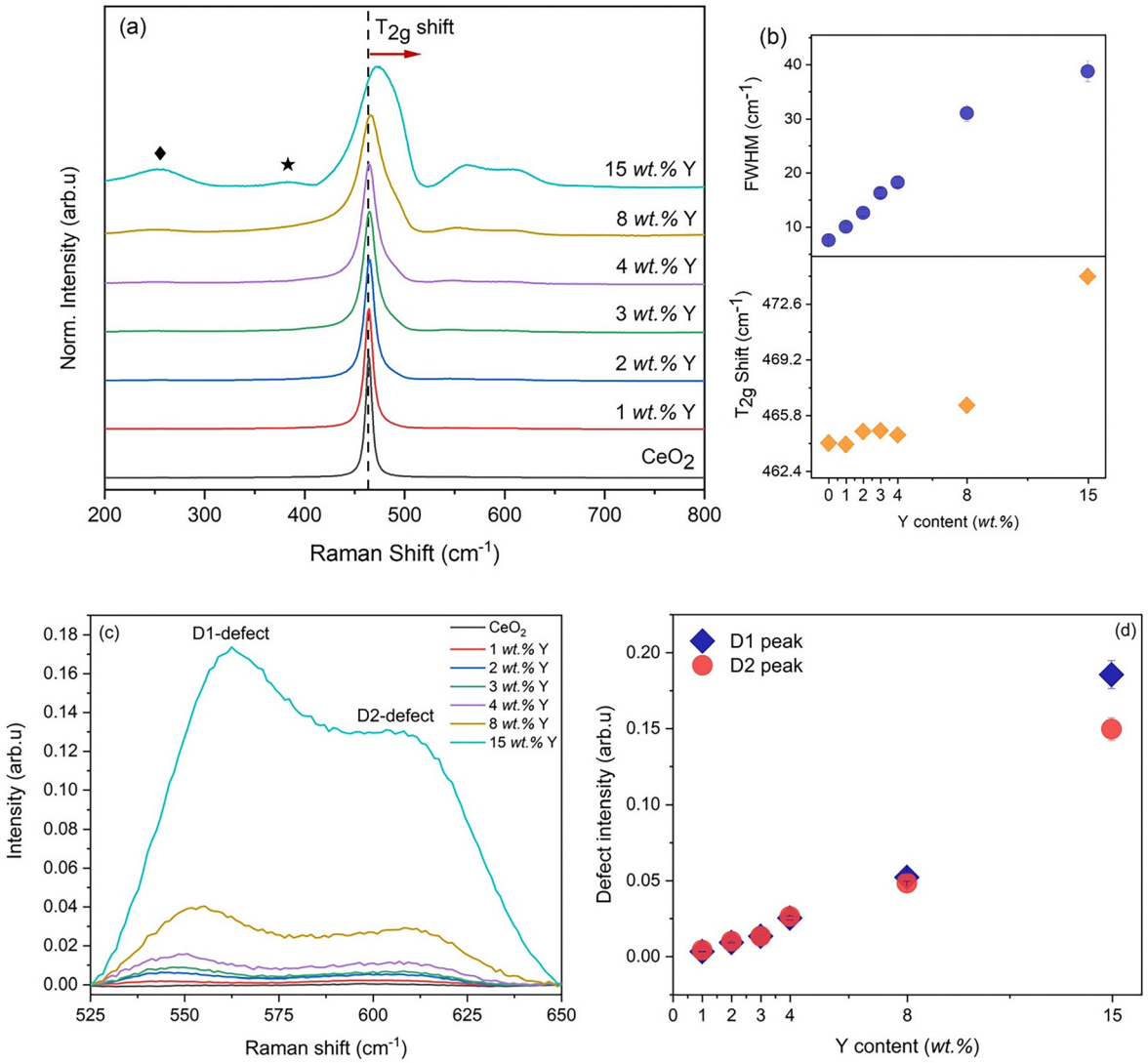

Fig. 4 (a) and (b) Raman spectra of sintered undoped and doped-CeO_2 pellets, showing the broadening and shift of the main T_{2g} peak. (c) and (d) The evolution of the defect D_1 (Y^{3+}-V_O) and D_2 (Ce^{3+}-V_O) peaks and the kinetic behaviour of the defect bands relative to the T_{2g} peak with increasing dopant content.

that alter the normal vibrational modes. The D_1 band is thus believed to originate from oxygen vacancy-type defects that break the O_h (octahedral) symmetry.[28]

Several interpretations of the D_2 band have been put forth. Nakayama *et al.*[29] ascribed this peak to intrinsic oxygen vacancies induced by the possible occurrence of Ce^{3+} given the redox CeO_2 character in sintering conditions used in this study, *i.e.*, Ce^{3+}-V_O defects. This agrees with studies carried out on Rh-, Gd- and Pr-doped CeO_2.[30] However, other authors argued that this band might be indicative to MO_8 (M = dopant cation) nanoclusters, without associated oxygen vacancies. This MO_8 environment has been reported for Sm/La-doped CeO_2[31] and most recently in Zr-doped UO_2.[32] Considering the redox CeO_2 character and PAS findings, it is more appropriate to assign the D_2 band to intrinsic Ce^{3+}-V_O defects in this work (*i.e.* $\{Ce^{\bullet} - V_O'' - Ce^{\bullet}\}^X$). Both extrinsic ($D_1$) and intrinsic ($D_2$) defect bands increase upon doping, and they behave similarly at low dopant content (<4 wt%), above which the Y^{3+}-V_O defects become prevalent. This observation adds to the evidence that the D_1 band is of extrinsic character and directly related to Y^{3+} doping.

3.2 Characterisation of irradiation-induced defect chemistry in $(Ce_{1-x}Y_x)O_{2-x/2}$

The CeO_2 and doped compositions maintained their fluorite crystallographic structure even after accumulating high damage levels (SI). These findings confirm the excellent radiation stability of fluorite-structured materials. No irradiation-induced amorphisation is observed, but Au-irradiation affects the lattice as illustrated by the behaviour of the (111) reflection of the 15 wt% Y-doped CeO_2 (Fig. 5). The fairly symmetrical X-ray peak broadens and can be deconvoluted using two fitting functions. The peak close to ~28.58°, *i.e.*, the initial position of the symmetrical (111) reflection before irradiation, corresponds

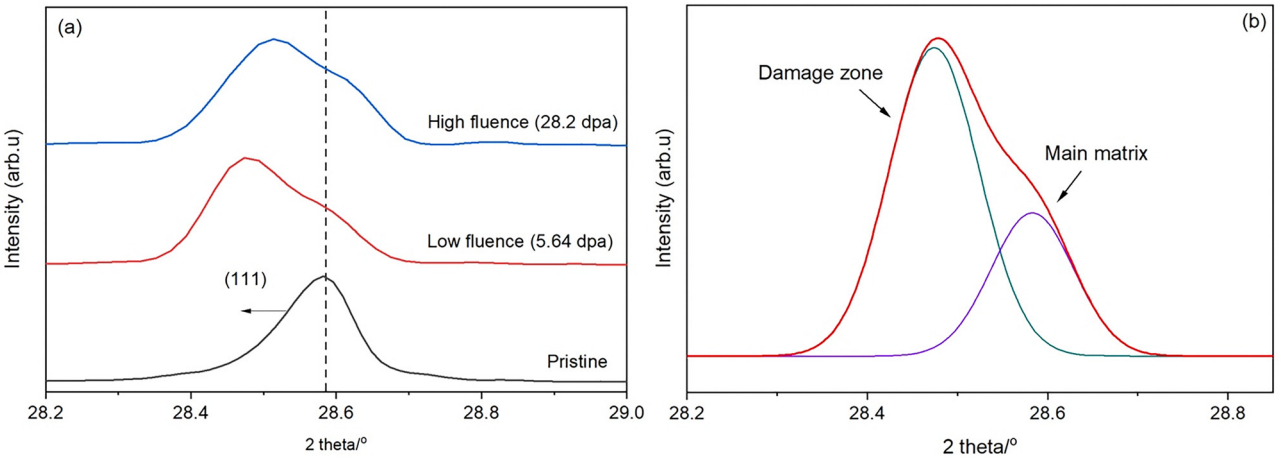

Fig. 5 (a) Au-ions irradiation-induced modifications of the main reflection for the 15 wt% Y-doped sample at low and high fluences, and (b) deconvolution of the asymmetrical (111) peak into the host Ce–O matrix and irradiation damage region.

to the main CeO_2 matrix. The additional peak at higher *d*-spacing, on the other hand, characterises the damaged zone.[33] Furthermore, irradiation-induced lattice swelling is noted as the (111) reflection shifts to lower 2θ values.

Au-irradiation distorts the local structure of pure fluorite-type materials and causes a breakdown of the Raman-active selection rules, leading to additional features in the 510–620 cm^{-1} spectral range as observed for UO_2 and PuO_2.[34–36] These new features have commonly been referred to as the irradiation defect band. Similar defect bands were reported by Ohhara *et al.*[37] during the *in situ* measurements of CeO_2 under 200 MeV Au-irradiation and their origin was assigned to disorders in both cationic and anionic sublattices. No such observations were made for the undoped CeO_2 in the current study (Fig. 6), which could be linked to the *ex situ* characterisation methods. Indeed, the system may have already initiated lattice recovery *via* defect recombination and reached a quasi-steady state at the characterisation stage. As a result, the residual defect concentration is not sufficient to induce a significant CeO_2 local symmetry lowering to be seen on the Raman spectra.

No new irradiation-induced peaks were observed for the doped compositions, but Au-implants caused a subtle increase of both D_1 and D_2 intensity (Fig. 6b). As previously discussed, these bands are characteristics of anionic defects formed to compensate for the charge due to Y^{3+} and Ce^{3+}. An increase in their relative intensity is thus indicative of an increase in the concentration of these defect-types upon irradiation.

This was further confirmed by PAS of the irradiation samples which reveal that ion irradiation induces more vacancy-type defects than the doping effect. For the undoped CeO_2 irradiated to 5.64 dpa, the positron results show the presence of two regions, extending to 0.4 and 1.2 μm from the surface and labelled "top" and "deep," respectively (Fig. 3b). According to

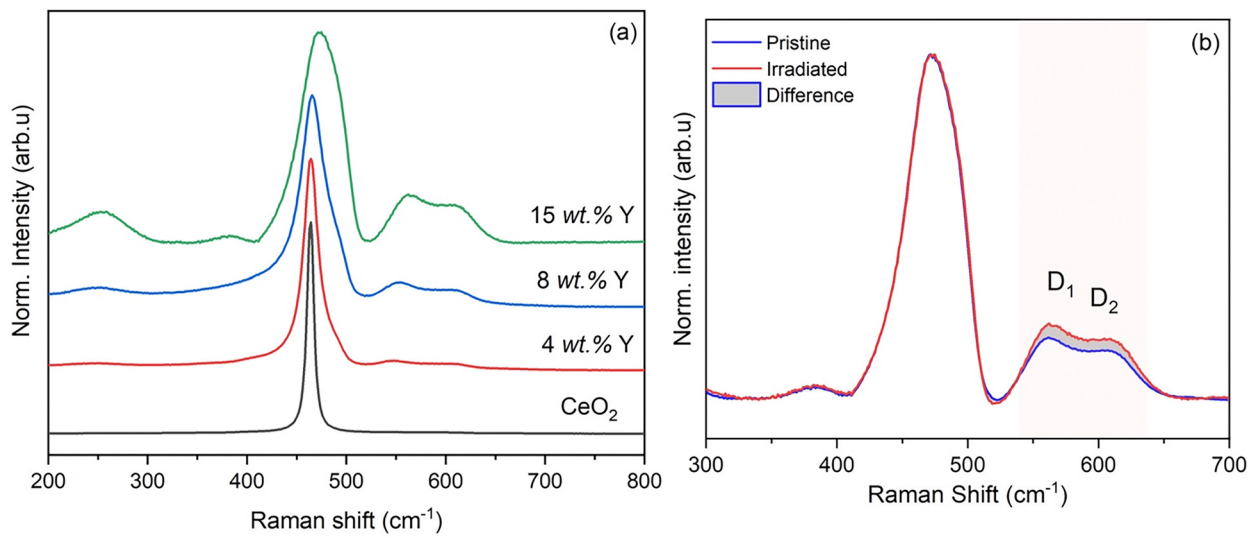

Fig. 6 (a) Post-irradiation Raman spectra for samples irradiated at high fluence (28.2 dpa) and (b) comparison of the pristine (unirradiated) and irradiated Raman spectra of the 15 wt% Y-doped sample showing the changes in the defect band region caused by Au-implants.

SRIM and TRIM simulations, the incident ions produce a maximum vacancy defect concentration at a depth between 0.1 and 0.3 μm, identified by the 6% increase in the low momentum *S*-parameter when compared to pristine CeO_2. The deeper region of the CeO_2 implanted at the higher dose of 28.2 dpa exhibits similar positron behaviour as the 5.64 dpa sample and correlates to the saturation trapping of positrons at vacancy sites. However, in the top region near the surface, the *S* values increase slightly but the *W* values decrease more significantly, resulting in changes in the slope on the *SW* plot. This suggests that at the higher dose, a different defect type was present.

The correlation between *S* and *W* parameters as a function of dopant concentration for the unirradiated samples reveals a shallower gradient than the *SW* correlation for the undoped CeO_2 with increasing damage. The irradiated Y-doped materials reside between these, suggesting that different annihilation sites were present, combining irradiation damage (open volume) and defects arising from Y-doping. This disparity in gradient slopes (m_{doped} = −0.286 for Y-doping and $m_{irradiated}$ = −0.69 for irradiation, respectively) shows that separate mechanisms contribute to defect formation. This can be explained by an increase in the number of defects detected or by a change in their nature, in particular by the formation of larger cluster regions due to displacements in both sublattices.

4. Discussion

Lattice changes caused by Au-implants to the host structure are shown on the distortions of the XRD patterns (Fig. 5) and are correlated to the induction of the irradiation defects. The partial reduction of CeO_2 post-irradiation was also noted. This redox character of CeO_2 has previously been reported under both light- and heavy-ion irradiation by means of X-ray photoelectron spectroscopy.[38] In the present study, Raman spectroscopy provided an alternative characterisation tool in identifying this defect redox chemistry by referring to the D_1 and D_2 peaks, which are associated with anionic defects and Ce^{3+}, respectively. The increased oxygen vacancy concentration is unsurprising as the anionic sublattice is more susceptible to damage, owing to the difference in the threshold displacement energy values of 27 and 56 eV for O and Ce atoms, respectively,[39] but the change in the D_2 peak intensity also confirms the subsequent accumulation of Ce^{3+} in the irradiated matrix.

Cureton *et al.*[40] reported a secondary triclinic $Ce_{11}O_{22}$ phase after the Au-irradiation of CeO_2 nanocrystalline materials. This behaviour was assigned to the CeO_2 redox behaviour, and ion-track formation as the oxygen segregation distance (20 nm) causes an accelerated loss of oxygen from the grains to void spaces or grain boundaries. However, no such observation is revealed by the XRD and Raman data in the current study. The latter may be attributed to a microstructural effect (average grain size of undoped CeO_2 was 8.74 ± 0.40 μm) and reduced defects mobility as irradiation was carried out at room temperature. Oxygen transport from grains to boundary areas is restricted and remains in the system, thus preventing the formation of an oxygen-deficient environment. Similar observations were recorded for the doped compositions. Y-addition degrades the host microstructure (grain size for the highest doped sample was found to be 1.02 ± 0.31 μm), but these changes were not enough to initiate secondary Ce-reduced phases formation, as reported for nanocrystalline materials, at least at the dopant concentration considered in this study.

Thus, the irradiation-induced swelling determined by the change in lattice parameters as a result of Au-irradiation, illustrated in Fig. 7 and Table 1, is due to the combined effects of both sublattice displacements and increased Ce^{3+} concentration (rCe^{3+} [C.N.:8] = 1.14 Å compared to rCe^{4+} [C.N.:8] = 0.97 Å).[19] The effect of Y-doping on the structural irradiation stability of CeO_2 was assessed by considering the overall change in lattice

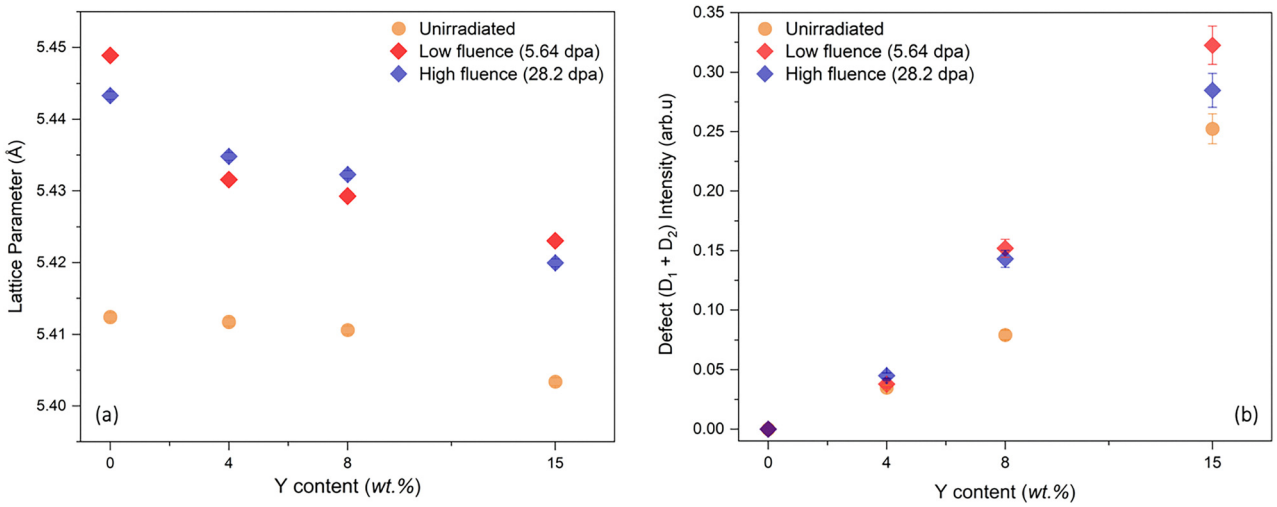

Fig. 7 Changes in (a) lattice parameter and (b) intensity of the defect D-bands for the undoped and doped Ce-based oxides before and after irradiation at low and high fluences.

Table 1 Degree of irradiation-induced swelling (%) determined from the increase in lattice parameters of the considered Ce-compositions before and after irradiation with Au-implants at low (5.64 dpa) and high (28.2 dpa) fluences

Y content (wt%)	0 (Pure CeO_2)	4 wt%	8 wt%	15 wt%
Low fluence (5.64 dpa)	67.4	36.63	34.5	36.4
High fluence (28.2 dpa)	57.1	42.6	40.1	30.7

parameters caused by ionic implantation. The undoped CeO_2 exhibits the greatest degree of irradiation-induced lattice expansion, but the swelling decreases with Y-doping as seen for the two Au-irradiation fluences, implying that trivalent doping improves the CeO_2 lattice resistance to radiation damage. Ivanov *et al.*[41] recently reported similar behaviour on CeO_2 microparticles implanted with Xe-ions, hence supporting our experimental findings. However, the authors could not ascertain the specific mechanisms underlying these observations.

The observed behaviour in Fig. 7 could be linked to the intrinsic changes that the dopant causes to the CeO_2 lattice. The direct cationic Y^{3+} substitution onto Ce-sites, the induction of both Ce^{3+} and Vo and the formation of Y_2O_3 nanodomains have implications on the local chemical bonding that affects the host lattice equilibrium. This results in a defective CeO_2 structure that is more prone to damage buildup. The introduction of Au-induced lattice defects would imply that the defective systems will accumulate a higher effective defect concentration compared to the undoped CeO_2, which can easily reach disorder saturation. Thus, excess defects will enable different recombination pathways, allowing for a more rapid lattice recovery that involves the migration and recombination of interstitial atoms and vacancies in the short-range volume order. This argument is supported by the fact that all samples were investigated in the ballistic regime of the incident ions, and the damaged region is contained within a relatively small volume (~250 nm). This therefore leads to a less damaged atomic structure when the doping element is considered.

An increase in the dopant content has little to no significant effect in further improving the radiation-induced swelling. When compared to low-doped samples, the high intrinsic disorder contained in the highly doped CeO_2 only facilitates the system to reach the defect saturation stage upon irradiation. This enhances the recombination volume and thus accelerates the lattice recovery mechanisms, until a defect equilibrium concentration is reached. Since only post-irradiation measurements were carried out, the data reported most likely characterise a stage where the defect recovery has already been initiated and reached a quasi-equilibrium residual defect concentration. Hence, the difference in defect recovery rates as a function of Y-content could not be quantified. *In situ* Raman or transmission electron microscopy (TEM) methods could better help to quantify the defect recombination kinetics by characterising the real-time migration and removal of lattice defects during ionic implantation.

The effect of irradiation dose on the defect mechanisms was also investigated. Interestingly, the lattice parameter and Raman defect bands do not differ much for the two considered Au-fluences. Positron measurements also showed similar trends. A significant increase in the *S*-parameter was expected

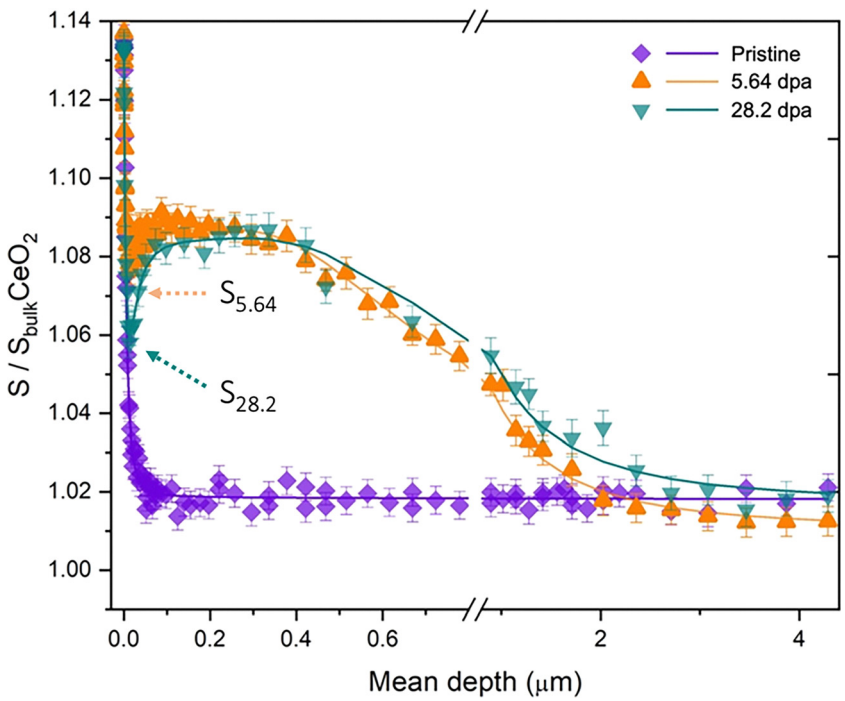

Fig. 8 Comparison of the *S*-parameter evolution as a function of depth for the 15 wt% doped CeO_2 pre- and post-irradiation, highlighting the specific role of the sample surface acting as defect sinks.

for the compositions irradiated to 28.2 dpa, but Fig. 3b showed that samples implanted at low fluence (5.64 dpa) have slightly higher *S*-values. This suggests that the concentration of lattice damage resulting from the lower irradiation fluence is close to the disorder saturation level, where all the implanted positrons are trapped. A higher irradiation dose will hence have no consequence on the positron measurement. In addition, the fact that the higher fluence causes a layer with SW on a different slope suggests that a larger (at least different) open volume defect is formed either by coalescence of defects during irradiation or by an increase in the likelihood to generate large (or different) defect clusters. It is important to note that distinguishing between these defect types is beyond the scope of this work and necessitates additional research, such as electron irradiation coupled with theoretical calculations to analyse specific lattice defects resulting from displacements in either Ce or O sublattice. The higher fluence study was also seen to induce important changes near the surface. This was more evident when looking at the highly defective lattice (CeO_2 doped with 15 wt% Y) as shown in Fig. 8, where the *S*-parameter at 5.64 dpa was greater than that at 28.2 dpa at depth below 50 nm. This could be indicative of a substantial dynamic damage recovery in this region and considerable defect migration to the surface, which serves as an effective sink for trapping mobile defects.

5. Conclusions

Experimental methods were employed to explore the effect of trivalent doping and irradiation effects on the stability of the fluorite CeO_2 structure. Initial XRD measurements of $Ce_{1-x}Y_xO_{2-x/2}$ solid solutions revealed that the dopant leads to a contraction of the unit cell which was attributed to long-range ordering of anionic vacancies with randomly distributed Y_2O_3 nanodomains of C-type configuration that grow coherently within the host matrix. Raman spectroscopy quantified the formation of oxygen vacancies to maintain charge neutrality as a result of direct cationic substitution and Ce^{3+} induction. The nature of these vacancy defects was further studied using positron annihilation spectroscopy, revealing they were associated with neutrally charged complex defect structures.

Post-irradiation characterisation validated the high radiation stability of Ce-based fluorite compounds for the fluences considered in this work, and Y-doping was found to improve the CeO_2 resistance to radiation damage in the ballistic regime of incident Au-ions. This behaviour was linked to the intrinsic alterations that the dopant imparts to the lattice that are believed to increase the defect recombination volume and facilitate improved lattice recovery. Furthermore, positrons revealed preferential defect migration and annealing near the sample surface as well as the possibility of a larger open volume defect, such as vacancy dislocations and clusters, or a completely different defect type that forms in the higher fluence case study. This mechanism was not observed under low fluence irradiation conditions.

Conflicts of interest

There are no conflicts to declare.

Data availability

All data files collected and processed as part of this research work are included in the manuscript as well as uploaded as supplementary figures. Supplementary information (SI) is available. See DOI: https://doi.org/10.1039/d5cp01848j.

The raw files can be made available upon request and with consent from all academic/institutional collaborators and funders involved in this work.

Acknowledgements

The authors acknowledge the Engineering and Physical Sciences Research Council for funding this research, under the UK–US Nuclear Energy University Programme (EP/R006075/1). This research was performed at the MIDAS Facility at the University of Sheffield established with financial support from EPSRC and BEIS, under grant EP/T011424/1. The US portion of the research was funded by the U.S. Department of Energy in support of the Nuclear Energy University Program – Used Nuclear Fuel Disposition program, award #DE-NE0008689. CLC is grateful to EPSRC for the award of an ECR Fellowship under grant number EP/N0117374/1. JM and MW would like to thank the US–UK Fulbright Commission for personal financial support during the research period. JM and MW would like to thank the S. Y. Chung Centenary Fellowship for support during the research period. SCM is supported through the Sêr Cymru II programme by the Welsh European Funding Office (WEFO) under the European Development Fund (ERDF). SCM is also supported through the EPSRC Enhanced Methodologies for Advanced Nuclear System Safety (eMEANSS – EP/T016329/1) project. The authors would also like to thank the Uranic Innovation Centre for its financial support, as well as the UKNNL's contribution.

References

1 H. Inaba and H. Tagawa, Ceria-based solid electrolytes, *Solid State Ionics*, 1996, **83**, 1–16, DOI: 10.1016/0167-2738(95)00229-4.

2 M. Mogensen, N. Sammes and G. Tompsett, Physical, chemical and electrochemical properties of pure and doped ceria, *Solid State Ionics*, 2000, **129**, 63–94, DOI: 10.1016/S0167-2738(99)00318-5.

3 D. A. Andersson, S. I. Simak, N. V. Skorodumova, I. A. Abrikosov and B. Johansson, Optimization of ionic conductivity in doped ceria, *Proc. Natl. Acad. Sci. U. S. A.*, 2006, **103**(10), 3518–3521, DOI: 10.1073/pnas.0509537103.

4 N. C. Hyatt, Safe management of the UK separated plutonium inventory: a challenge of materials degradation, *npj Mater. Degrad.*, 2020, 1–4, DOI: 10.1038/s41529-020-00132-7.

5 Z. Talip, *et al.*, Raman and X-ray Studies of Uranium-Lanthanum-Mixed Oxides before and after Air Oxidation, *J. Am. Ceram. Soc.*, 2015, **98**(7), 2278–2285, DOI: 10.1111/jace.13559.

6 C. Tian and S. Chan, Ionic conductivities, sintering temperatures and microstructures of bulk ceramic CeO_2 doped with Y_2O_3, *Solid State Ionics*, 2000, **134**, 89–102, DOI: 10.1016/S0167-2738(00)00717-7.

7 T. Mori and J. Drennan, Influence of Microstructure on Oxide Ionic Conductivity in Doped CeO_2, *J. Electroceram.*, 2006, **17**, 749–757, DOI: 10.1007/s10832-006-6311-7.

8 D. R. Ou, T. Mori, F. Ye, M. Takahashi, J. Zou and J. Drennan, Microstructures and electrolytic properties of yttrium-doped ceria electrolytes: Dopant concentration and grain size dependences, *Acta Mater.*, 2006, **54**, 3737–3746, DOI: 10.1016/j.actamat.2006.04.003.

9 D. R. Ou, T. Mori, F. Ye and T. Kobayashi, Oxygen vacancy ordering in heavily rare- earth-doped ceria, *Appl. Phys. Lett.*, 2006, **171911**, 87–90, DOI: 10.1063/1.2369881.

10 D. R. Ou, T. Mori, F. Ye, J. Zou, G. Auchterlonie and J. Drennan, Oxygen-vacancy ordering in lanthanide-doped ceria: Dopant-type dependence and structure model, *Phys. Rev. B: Condens. Matter Mater. Phys.*, 2008, **77**(024108), 1–8, DOI: 10.1103/PhysRevB.77.024108.

11 H. Balboa, L. Van Brutzel, A. Chartier and Y. Le Bouar, Damage characterization of $(U,Pu)O_2$ under irradiation by Molecular Dynamics simulations, *J. Nucl. Mater.*, 2018, **512**, 440–449, DOI: 10.1016/j.jnucmat.2018.07.056.

12 R. Mohun, L. Desgranges, A. Canizarès, N. Raimboux, F. Duval, R. Omnee, C. Jégou, S. Miro and P. Simon, Investigating the role of irradiation defects during UO_2 oxidative dissolution, *J. Nucl. Mater.*, 2018, **509**, 305–312, DOI: 10.1016/j.jnucmat.2018.06.046.

13 T. Sonoda, M. Kinoshita, N. Ishikawa, M. Sataka, Y. Chimi, N. Okubo, A. Iwase and K. Yasunaga, Clarification of the properties and accumulation effects of ion tracks in CeO_2, *Nucl. Instr. and Meth. in Phys. Res. B*, 2008, **266**, 2882–2886, DOI: 10.1016/j.nimb.2008.03.214.

14 T. Sonoda, M. Kinoshita, Y. Chimi, N. Ishikawa, M. Sataka and A. Iwase, Electronic excitation effects in CeO_2 under irradiations with high-energy ions of typical fission products, *Nucl. Instrum. Methods Phys. Res., Sect. B*, 2006, **250**, 254–258, DOI: 10.1016/j.nimb.2006.04.120.

15 K. Yasunaga, K. Yasuda, S. Matsumura and T. Sonoda, Nucleation and growth of defect clusters in CeO_2 irradiated with electrons, *Nucl. Instrum. Methods Phys. Res., Sect. B*, 2006, **250**, 114–118, DOI: 10.1016/j.nimb.2006.04.091.

16 A. T. Nelson, D. R. Rittman, J. T. White, J. T. Dunwoody, M. Kato and K. J. McClellan, An Evaluation of the Thermophysical Properties of Stoichiometric CeO_2 in Comparison to UO_2 and PuO_2, *J. Am. Ceram. Soc.*, 2014, **97**(11), 3652–3659, DOI: 10.1111/jace.13170.

17 N. C. Hyatt, C. L. Corkhill, M. C. Stennett, R. J. Hand, L. J. Gardner and C. L. Thorpe, The HADES Facility for High Activity Decommissioning Engineering & Science: part of the UK National Nuclear User Facility, *IOP Conf. Ser.: Mater. Sci. Eng.*, 2020, **818**, 012022, DOI: 10.1088/1757-899X/818/1/012022.

18 J. F. Ziegler, M. D. Ziegler and J. P. Biersack, SRIM (Stopping and Range of Ions in Matter), *Nucl. Instrum. Methods Phys. Res., Sect. B*, 2010, **268**, 1818–1823, DOI: 10.1016/j.nimb.2010.02.091.

19 R. D. Shannon, Revised Effective Ionic Radii and Systematic Studies of Interatomic Distances in Halides and Chalcogenides, *Acta Crystallogr.*, 1976, **A32**, 751–767, DOI: 10.1107/S0567739476001551.

20 M. Coduri, S. Checchia, M. Longhi, D. Ceresoli and M. Scavini, Rare Earth Doped Ceria: The Complex Connection Between Structure and Properties, *Front. Chem.*, 2018, **6**(526), 1–23, DOI: 10.3389/fchem.2018.00526.

21 M. Coduri, M. Scavini, M. Allieta, M. Brunelli and C. Ferrero, Defect Structure of Y Doped Ceria on Different Length Scales, *Chem. Mater.*, 2013, **25**, 4278–4289, DOI: 10.1021/cm402359d.

22 T. Mori, J. Drennan, Y. Wang, G. Auchterlonie, J.-G. Li and A. Yago, Influence of nano-structural feature on electrolytic properties in Y_2O_3 doped CeO_2 system, *Sci. Technol. Adv. Mater.*, 2003, **4**, 213–220, DOI: 10.1016/S1468-6996(03)00047-0.

23 M. Coduri, M. Scavini, M. Allieta, M. Brunelli and C. Ferrero, Local disorder in yttrium doped ceria ($Ce_{1-x}Y_xO_{2-x}/2$) probed by joint X-ray and Neutron Powder Diffraction, *J. Phys.: Conf. Ser.*, 2012, **012056**(340), DOI: 10.1088/1742-6596/340/1/012056.

24 R. Mohun, L. Desgranges, C. Jégou, B. Boizot, O. Cavani, A. Canizarès, F. Duval, C. He, P. Desgardin, M.-F. Barthe and P. Simon, Quantification of irradiation-induced defects in UO_2 using Raman and positron annihilation spectroscopies, *Acta Mater.*, 2019, **164**, 512–519, DOI: 10.1016/j.actamat.2018.10.044.

25 N. Paunović, Z. Dohčević-Mitrović, R. Scurtu, S. Aškrabić, M. Prekajski, B. Matović and Z. V. Popović, Suppression of inherent ferromagnetism in Pr-doped CeO_2 nanocrystals, *Nanoscale*, 2012, **4**, 5469–5476, DOI: 10.1039/c2nr30799e.

26 M. Guo, J. Lu, Y. Wu, Y. Wang and M. Luo, UV and visible Raman studies of oxygen vacancies in rare-earth-doped ceria, *Langmuir*, 2011, **27**(7), 3872–3877, DOI: 10.1021/la200292f.

27 J. McBride, K. Hass, B. Poindexter and W. Weber, Raman and X-ray studies of $Ce_{1-x}RE_xO_{2-y}$, where RE = La, Pr, Nd, Eu, Gd, and Tb, *J. Appl. Phys.*, 1994, **4**(76), 2435–2441, DOI: 10.1063/1.357593.

28 D. Avram, M. Sanchez-Dominguez, B. Cojocaru, M. Florea, V. Parvulescu and C. Tiseanu, Toward a Unified Description of Luminescence − Local Structure Correlation in Ln Doped CeO_2 Nanoparticles: Roles of Ln Ionic Radius, Ln Concentration, and Oxygen Vacancies, *J. Phys. Chem. C*, 2015, **119**, 16303–16313, DOI: 10.1021/acs.jpcc.5b02240.

29 M. Nakayama and M. Martin, First-principles study on defect chemistry and migration of oxide ions in ceria doped

with rare-earth cations, *Phys. Chem. Chem. Phys.*, 2009, **11**, 3241–3249, DOI: 10.1039/B900162J.

30 A. M. D'Angelo and A. L. Chaffee, Correlations between Oxygen Uptake and Vacancy Concentration in Pr-Doped CeO_2, *ACS Omega*, 2017, **2**, 2544–2551, DOI: 10.1021/acsomega.7b00550.

31 D. Mukherjee, B. G. Rao and B. M. Reddy, Characterization of Ceria-Based Nano-Oxide Catalysts by Raman Spectroscopy, *Top. Catal.*, 2017, **60**(19), 1673–1681, DOI: 10.1007/s11244-017-0846-5.

32 J. Lee, J. Kim, Y.-S. Youn, N. Liu, J.-G. Kim, Y.-K. Ha, D. W. Shoesmith and J.-Y. Kim, Raman study on structure of $U_{1-y}Gd_yO_{2-x}$ (y = 0.005, 0.01, 0.03, 0.05 and 0.1) solid solutions, *J. Nucl. Mater.*, 2017, **486**, 216–221, DOI: 10.1016/j.jnucmat.2017.01.004.

33 N. Ishikawa, Y. Chimi, O. Michikami, Y. Ohta, K. Ohhara, L. Lang and R. Neumann, *et al.*, Study of structural change in CeO_2 irradiated with high-energy ions by means of X-ray diffraction measurement, *Nucl. Instrum. Methods Phys. Res., Sect. B*, 2008, **266**(12–13), 3033–3036, DOI: 10.1016/j.nimb.2008.03.159.

34 R. Mohun, *et al.*, Charged defects during alpha-irradiation of actinide oxides as revealed by Raman and luminescence spectroscopy, *Nucl. Instrum. Methods Phys. Res., Sect. B*, 2020, **374**, 67–70, DOI: 10.1016/j.nimb.2015.08.003.

35 G. Guimbretière, A. Canizarès, N. Raimboux, J. Joseph, P. Desgardin, L. Desgranges, C. Jegou and P. Simon, High temperature Raman study of UO_2: A possible tool for in situ estimation of irradiation-induced heating, *J. Raman Spectrosc.*, 2015, **46**(4), 418–420, DOI: 10.1002/jrs.4661.

36 M. Sarsfield, R. Taylor, C. Puxley and H. Steele, Raman spectroscopy of plutonium dioxide and related materials, *J. Nucl. Mater.*, 2012, **427**, 333–342, DOI: 10.1016/j.jnucmat.2012.04.034.

37 K. Ohhara, *et al.*, Oxygen defects created in CeO2 irradiated with 200 MeV Au, The Seventh International Symposium on Swift Heavy Ions in Matter, p. Lyon, France, 2008.

38 K. Maslakov, *et al.*, Applied Surface Science XPS study of ion irradiated and unirradiated CeO_2 bulk and thin film samples, *Appl. Surf. Sci.*, 2018, **448**, 154–162, DOI: 10.1016/j.apsusc.2018.04.077.

39 A. Guglielmetti, A. Chartier, L. Van Brutzel, J.-P. Crocombette, K. Yasuda, C. Meis and S. Matsumura, Atomistic simulation of point defects behavior in ceria, *Nucl. Instrum. Methods Phys. Res., Sect. B*, 2008, **266**(24), 5120–5125, DOI: 10.1016/j.nimb.2008.09.010.

40 W. Cureton, *et al.*, Grain size effects on irradiated CeO_2, ThO_2, and UO_2, *Acta Mater.*, 2018, **160**, 47–56, DOI: 10.1016/j.actamat.2018.08.040.

41 I. A. Ivanov, R. M. Rspayev, A. D. Sapar, D. A. Mustafin, M. V. Zdorovets and A. L. Kozlovskiy, Study of the effect of Y_2O_3 doping on the resistance to radiation damage of CeO_2 microparticles under irradiation with heavy Xe^{22+} ions, *Crystals*, 2021, **11**(12), 1459, DOI: 10.3390/cryst11121459.